Navier-Stokes Simulations of Rotor/Stator Interaction Using Patched and Overlaid Grids

Man Mohan Rai*
NASA Ames Research Center, Moffett Field, California

An accurate numerical analysis of the flows associated with rotor/stator configurations in turbomachinery can be very helpful in optimizing performance. In this study, the unsteady, thin-layer, Navier-Stokes equations are solved using a system of patched and overlaid grids for a rotor/stator configuration of an axial turbine. The equations necessary for an accurate transfer of information between the several grids are briefly described within the framework of an iterative, implicit algorithm. Results in the form of Mach number contours, time-averaged pressures, unsteady pressures, amplitudes, and phase are presented. The numerical results are also compared with experimental data and the agreement is found to be good.

Introduction

THE aerodynamic processes associated with the flow of fluid through turbomachines pose one of the toughest challenges to the computational fluid dynamicist. The unsteady nature of the flow, the complex geometries involved, the motion of some parts of the system relative to others, and the periodic transition of the flow from laminar to turbulent are some of the factors that contribute to the complexity of the problem. A clear understanding of these types of flows is essential for the optimization of the performance of turbomachinery. In this study, an attempt is made to analyze two-dimensional flow past the rotor/stator configuration of an axial turbine using state-of-the-art computational tools and computing facilities.

The two-dimensional analysis of stator airfoils in isolation or rotor airfoils in isolation is a relatively straightforward task. Such an analysis is valid when the two rows of blades are set far enough apart so that the interaction effects are minimal. However, the desire to minimize engine length requires the stator and rotor airfoils to be closely spaced. Clearly, the interaction effects will become more important as the axial gap between the rows is reduced. In fact, the flow becomes periodically unsteady for small values of the axial gap. The experimental results of Ref. 1 show that the temporal pressure fluctuation (the difference between the minimum and maximum pressure values) near the leading edge of the rotor can be as much as 72% of the exit dynamic pressure when the axial gap is reduced to 15% of the chord length (for the operating conditions and geometry chosen). Hence, it is important that the rotor and stator airfoils be treated as a single system when the interaction effects become predominant. A computational tool that provides the design engineer with the necessary aerodynamic data can be used to great advantage in redesigning rotor and stator airfoils to enhance performance. Such a tool has to accurately simulate the unsteady flow associated with rotor/stator configurations exhibiting a strong interaction.

A finite-difference solution to the Navier-Stokes equations requires the generation of a computational grid for the geometry of interest. The generation of a single grid for regions containing multiple bodies is not a simple task. In fact, in many cases it is impractical, if not impossible, to generate a single grid for the region of interest. The grid generation procedure is even more complicated when some of these multiple bodies move relative to each other. An alternative to the "single-grid" approach is the "multiple-grid" approach. In the multiple-grid approach, the calculation is performed on several grids that are either patched together as in Fig. 1a or overlaid as in Fig. 1b. For the computational fluid dynamicist, an important consideration in calculations with multiple grids is the accurate transfer of information from one grid to another. The finite-difference equations used to effect this information transfer must satisfy several requirements before they can be used effectively. The equations must be 1) numerically stable, 2) spatially and temporally accurate, 3) conservative so that flow discontinuities can move from one grid to another without any distortion, and 4) easily applicable in generalized coordinates.

Recent efforts in the use of multiple grids for solving geometrically complex problems[2-5] indicate that performing calculations on multiple grids (both patched and overlaid) using the Euler equations is possible. However, the flexibility that they provide in treating complex topologies is obtained at the expense of programming simplicity.

References 2-4 deal with the treatment of patched grids. In the patched-grid technique, the different "patches" or "zones" are separated by common boundaries called patch boundaries. The grid points on these patch boundaries need to be treated with care so that the requirements mentioned earlier (numerical stability, accuracy, and conservation across patch boundaries) are satisfied. A patch boundary condition that meets these requirements is developed in Refs. 2-4. In Ref. 2, a conservative patch boundary condition is developed for explicit, first-order accurate integration schemes as applied to the Euler equations. This patch boundary scheme is extended to implicit, second-order accurate integration schemes in Ref. 3. The feasibility of performing calculations on grids that move relative to each other and the equations necessary to maintain time accuracy (in addition to the usual requirement of spatial accuracy) at the patch boundary are also developed in Ref. 3. Reference 4 gives the extension of the explicit patched-grid scheme to relaxation schemes (as opposed to the approximately factored implicit schemes used in Ref. 3). Preliminary results for a simple rotor/stator configuration are also presented in Ref. 4.

One aspect of rotor/stator configurations not represented in the results of Ref. 4 is the effect of the aft airfoil on the

Presented as Paper 85-1519 at the AIAA 7th Computational Fluid Dynamics Conference, July 15-17, 1985, Cincinnati, OH; received Sept. 27, 1985; revision received Sept. 16, 1986.

*Research Scientist. Member AIAA.

forward airfoil (the supersonic nature of the flow does not permit such an interaction). However, the patch boundary conditions were implemented so that an interaction would be accounted for if it were present. The present calculation, using the blade geometry of Ref. 1 and purely subsonic flow in the region of interest, tests the capability of the zonal scheme in accurately simulating such an interaction.

Reference 5 deals with the use of overlaid grids in solving the Euler equations. Encouraging results are presented for several example problems. However, the issues of time accuracy and conservation are not addressed in Ref. 5. This study will include the necessary extensions to the overlaid grid technique of Ref. 5 in order to make it time accurate.

Both patched and overlaid grid concepts have their relative strengths and weaknesses. In the patched-grid approach, conservation can be easily maintained at the patch interfaces (even in the case of grids that move relative to each other). The extra computing time required to implement the zonal boundary condition is less than that required for overlaid grids. This is because the necessary interpolations effecting the information transfer between zones are performed in a reduced number of spatial dimensions for patched grids. A problem in two dimensions requires interpolation in one dimension; similarly, a problem in three dimensions requires only a two-dimensional interpolation procedure. This reduction in the number of dimensions in which the interpolation is performed does not occur for overlaid grids. This may be a critical factor in situations where information needs to be transferred between two overlaid grids that move relative to each other (the interpolation coefficients have to be calculated at each time step, thus increasing computing costs considerably). On the other hand, overlaid grids provide more flexibility in generating grids because there are fewer constraints on the choice of the outer boundaries for the different zones.

In this study, both the patched and overlaid grid techniques are used to simulate the flow associated with the rotor/stator configuration of Ref. 1. The thin-layer, time-dependent Navier-Stokes equations in two spatial dimensions are solved using a variant of the Beam-Warming scheme[6] developed in Ref. 7. Comparisons with the experimental data of Ref. 1 are also made. The comparisons include time-averaged values of surface pressure, pressure amplitudes, and phase relationships.

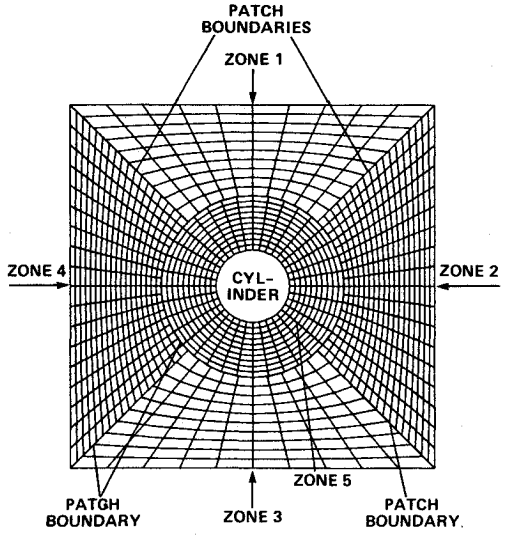

a) Patched grid.

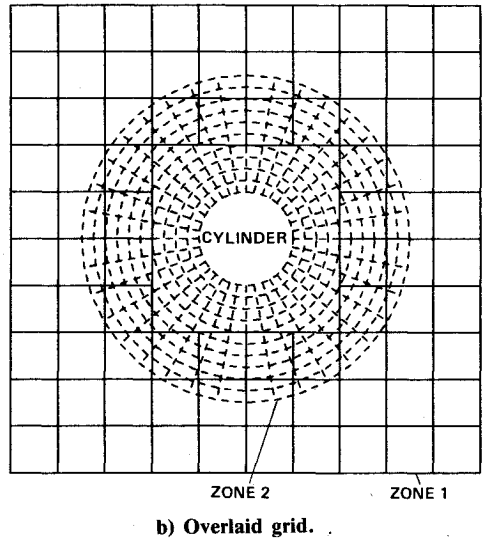

b) Overlaid grid.

Fig. 1 Use of multiple grids in finite-difference calculations.

Integration Method

The integration scheme used is an iterative, factored, implicit algorithm developed in Ref. 7. To describe the scheme we consider the unsteady Navier-Stokes equations in two dimensions,

$$Q_t + E_x + F_y = R_x + S_y \tag{1}$$

where

$$Q = \begin{bmatrix} \rho \\ \rho u \\ \rho v \\ e \end{bmatrix}, \quad E = \begin{bmatrix} \rho u \\ p + \rho u^2 \\ \rho uv \\ (e+p)u \end{bmatrix}, \quad F = \begin{bmatrix} \rho v \\ \rho uv \\ p + \rho v^2 \\ (e+p)v \end{bmatrix} \tag{2a}$$

$$R = \begin{bmatrix} 0 \\ \tau_{xx} \\ \tau_{xy} \\ \beta_x \end{bmatrix}, \quad S = \begin{bmatrix} 0 \\ \tau_{xy} \\ \tau_{yy} \\ \beta_y \end{bmatrix} \tag{2b}$$

and

$$\tau_{xx} = 2\mu u_x + \lambda(u_x + v_y)$$

$$\tau_{xy} = \mu(u_y + v_x)$$

$$\tau_{yy} = 2\mu v_y + \lambda(u_x + v_y)$$

$$\beta_x = u\tau_{xx} + v\tau_{xy} + \gamma\mu Pr^{-1}\tilde{e}_x$$

$$\beta_y = u\tau_{xy} + v\tau_{yy} + \gamma\mu Pr^{-1}\tilde{e}_y$$

$$\lambda = -2\mu/3$$

$$\tilde{e} = p/[\rho(\gamma - 1)] \tag{3}$$

Making the independent variable transformation

$$\tau = t, \quad \xi = \xi(x,y,t)$$

$$\eta = \eta(x,y,t) \tag{4}$$

and the thin-layer approximation,[8] we obtain

$$\tilde{Q}_\tau + \tilde{E}_\xi + \tilde{F}_\eta = Re^{-1}\tilde{S}_\eta \tag{5}$$

where

$$\tilde{Q} = Q/J$$

$$\tilde{E}(Q,\xi) = (\xi_t Q + \xi_x E + \xi_y F)/J$$

$$\tilde{F}(Q,\eta) = (\eta_t Q + \eta_x E + \eta_y F)/J$$

$$J = \xi_x \eta_y - \eta_x \xi_y \tag{6}$$

The vector $\tilde{S}$ is given by

$$\tilde{S} = \begin{bmatrix} 0 \\ K_1 u_\eta + K_2 \eta_x \\ K_1 v_\eta + K_2 \eta_y \\ K_1\{Pr^{-1}(\gamma-1)^{-1}(a^2)_\eta + [(u^2+v^2)/2]_\eta\} \\ + K_2(u\eta_x + v\eta_y) \end{bmatrix} \tag{7}$$

where

$$K_1 = \mu(\eta_x^2 + \eta_y^2)$$

$$K_2 = \mu(\eta_x u_\eta + \eta_y v_\eta)/3$$

Equations (5) and (7) assume that the body surface is a constant η line (in incorporating the thin-layer approximation).

The factored, iterative, implicit algorithm is given by

$$\left[I + \frac{\Delta\tau}{\Delta\xi}(\nabla_\xi \tilde{A}^+_{j,k} + \Delta_\xi \tilde{A}^-_{j,k})\right]^p \left[I + \frac{\Delta\tau}{\Delta\eta}(\nabla_\eta \tilde{B}^+_{j,k} + \Delta_\eta \tilde{B}^-_{j,k} - Re^{-1}\delta_\eta \tilde{M})\right]^p (\tilde{Q}^{p+1}_{j,k} - \tilde{Q}^p_{j,k})$$

$$= -\Delta\tau\left[\frac{\tilde{Q}^p_{j,k} - \tilde{Q}^n_{j,k}}{\Delta\tau} + \frac{\hat{E}^p_{j+\frac{1}{2},k} - \hat{E}^p_{j-\frac{1}{2},k}}{\Delta\xi} + \frac{\hat{F}^p_{j,k+\frac{1}{2}} - \hat{F}^p_{j,k-\frac{1}{2}}}{\Delta\eta} - \frac{\hat{S}^p_{j,k+\frac{1}{2}} - \hat{S}^p_{j,k-\frac{1}{2}}}{Re\Delta\eta}\right] \tag{8}$$

where

$$\tilde{A}^\pm = \left(\frac{\partial\tilde{E}}{\partial\tilde{Q}}\right)^\pm, \quad \tilde{B}^\pm = \left(\frac{\partial\tilde{F}}{\partial\tilde{Q}}\right)^\pm, \quad \tilde{M} = \frac{\partial\tilde{S}}{\partial\tilde{Q}} \tag{9}$$

and Δ, ∇, and δ are forward, backward, and central difference operators, respectively. The quantities $\hat{E}_{j+\frac{1}{2},k}$, $\hat{F}_{j,k+\frac{1}{2}}$, and $\hat{S}_{j,k+\frac{1}{2}}$ are numerical fluxes that are consistent with the physical fluxes $\tilde{E}$, $\tilde{F}$, and $\tilde{S}$. In Eq. (8), $\tilde{Q}^p$ is an approximation to $\tilde{Q}^{n+1}$. $\tilde{Q}^p = \tilde{Q}^n$ when $p=0$, and $\tilde{Q}^p = \tilde{Q}^{n+1}$ when Eq. (8) is iterated to convergence at any given time step. It should be noted that, because the left-hand side of Eq. (7) can be driven to zero at each time step (by iterating to convergence), linearization and factorization errors can be driven to zero during the iteration process. For problems where only the asymptotic steady state is of interest, the iteration process need not be carried to convergence at each time step. In fact, when the number of iterations is restricted to one, the scheme reverts to a conventional, noniterative scheme of the type in Ref. 6. When second-order accuracy in time is required, the term $(\tilde{Q}^p_{j,k} - \tilde{Q}^n_{j,k})$ on the right-hand side of Eq. (8) must be replaced by $(1.5\tilde{Q}^p_{j,k} - 2.0\tilde{Q}^n_{j,k} + 0.5\tilde{Q}^{n-1}_{j,k})$ in addition to iterating to convergence. Typically, three to four iterations per time step are sufficient to reduce the residual by an order of magnitude or more.

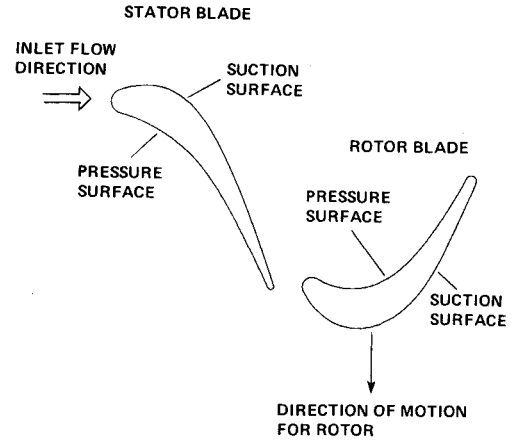

Fig. 2 Rotor/stator geometry of Ref. 1.

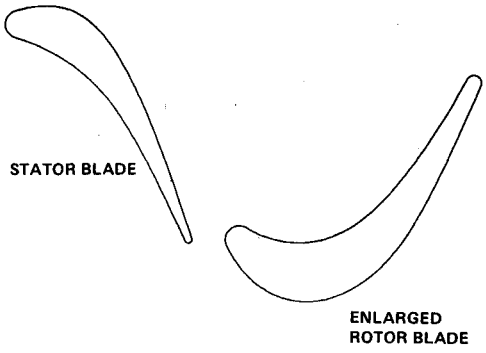

Fig. 3 Modified rotor/stator geometry.

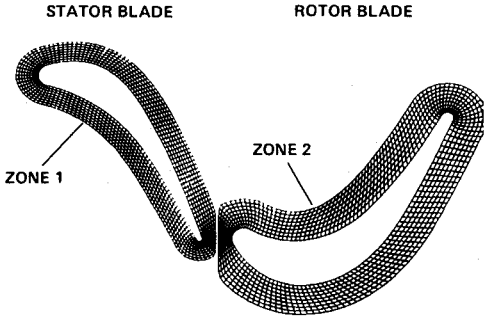

Fig. 4 "O"-type grids for zones 1 and 2.

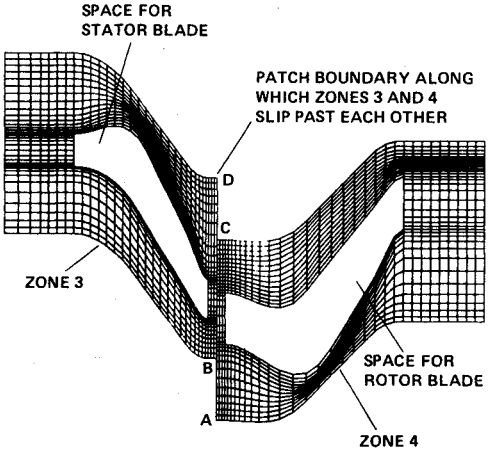

Fig. 5 Algebraically generated grids for zones 3 and 4.

Different choices for the numerical fluxes lead to different integration schemes. The central difference scheme used in this study can be obtained with the numerical fluxes defined as

$$\hat{E}_{j+\frac{1}{2},k} = \tfrac{1}{2}\left[\tilde{E}(Q_{j,k},\xi_{j+\frac{1}{2},k}) + E(Q_{j+1,k},\xi_{j+\frac{1}{2},k})\right]$$

$$\hat{F}_{j,k+\frac{1}{2}} = \tfrac{1}{2}\left[\tilde{F}(Q_{j,k},\eta_{j,k+\frac{1}{2}}) + \tilde{F}(Q_{j,k+1},\eta_{j,k+\frac{1}{2}})\right]$$

$$\hat{S}_{j,k+\frac{1}{2}} = \tilde{S}[Q_{j,k+\frac{1}{2}},(Q_\eta)_{j,k+\frac{1}{2}},\eta_{j,k+\frac{1}{2}}] \tag{10}$$

where

$$Q_{j,k+\frac{1}{2}} = \tfrac{1}{2}(Q_{j,k} + Q_{j,k+1})$$

$$(Q_\eta)_{j,k+\frac{1}{2}} = Q_{j,k+1} - Q_{j,k}$$

The smoothing terms necessary to stabilize the calculation were included in the numerical fluxes by redefining them to be

$$\hat{E}_{j+\frac{1}{2},k} = \tfrac{1}{2}\{\tilde{E}(Q_{j,k},\xi_{j+\frac{1}{2},k}) + \tilde{E}(Q_{j+1,k},\xi_{j+\frac{1}{2},k})$$

$$+\frac{\epsilon}{2}[\,|\Delta\tilde{E}(Q_{j-1,k},Q_{j,k},\xi_{j+\frac{1}{2},k})|$$

$$-2\,|\Delta\tilde{E}(Q_{j,k},Q_{j+1,k},\xi_{j+\frac{1}{2},k})|$$

$$+\,|\Delta\tilde{E}(Q_{j+1,k},Q_{j+2,k},\xi_{j+\frac{1}{2},k})|\,]\} \tag{11}$$

where

$$|\Delta\tilde{E}(Q_{j,k},Q_{j+1,k},\xi_{j+\frac{1}{2},k})|$$

$$= \left|\frac{\partial\tilde{E}}{\partial\tilde{Q}}(Q_{j+\frac{1}{2},k},\xi_{j+\frac{1}{2},k})\right|(\tilde{Q}_{j+1,k} - \tilde{Q}_{j,k}) \tag{12}$$

The numerical flux $\hat{F}_{j,k+\frac{1}{2}}$ is redefined in a similar manner. The advantage in including the smoothing term in the definition of numerical flux is that it can also be made conservative across the patch boundaries. The term ϵ in Eq. (11) determines the amount of smoothing used in the calculation, $\epsilon = 1$ corresponding to the amount of smoothing in a fully upwind scheme. Additional details of this smoothing parameter and the factored, iterative, implicit algorithm can be found in Refs. 3 and 7.

Grid System for the Rotor/Stator Configuration

The airfoil geometry of Ref. 1 is much more complicated than the simple circular-arc geometry used in Ref. 4. Figure 2 shows the shape of the rotor and stator airfoils and their orientation relative to each other and the inlet flow direction. The stator and rotor rows consisted of 22 and 28 airfoils, respectively. A Navier-Stokes calculation with a total of 50 airfoils would be extremely time consuming. To overcome this difficulty, the rotor airfoils were enlarged by a factor of 28/22, keeping the pitch-to-chord ratio the same. It was then assumed (for the calculation) that there were only 22 airfoils in the rotor row. This assumption made it possible to perform a calculation with only one rotor airfoil and one stator airfoil (a periodicity boundary condition was used to simulate the presence of the rest of the airfoils). The original stator and the modified rotor are shown in Fig. 3. The axial gap between them was chosen to be 15% of the average chord length.

This rotor/stator configuration and the associated flow region can be discretized by using only patched grids.

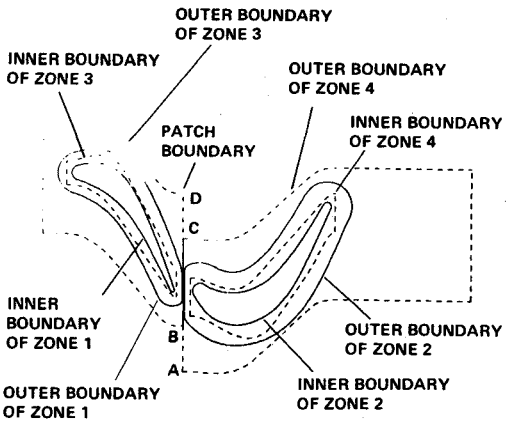

Fig. 6 Zoning of the rotor/stator problem showing patch and overlay boundaries.

However, the number of zones required to solve the problem accurately is twice as many as required when both patched and overlaid grids are used in conjunction with each other. Hence, a combination of patched and overlaid grids is used in this study.

The grid system chosen for the calculation consists of four different zones. The first zone contains the stator and is discretized with an "O" grid. The second zone contains the rotor and is also discretized with an "O" grid. These two zones do not overlap each other. The grids in zones 1 and 2 were generated using an elliptic grid generator of the type developed in Ref. 9 (these grids are shown in Fig. 4). The set of grid lines that intersect the airfoil surfaces is orthogonal to these surfaces. Although the actual grids used for the calculation are very dense near the airfoil surfaces (to resolve the viscous effects), for the purpose of clarity Fig. 4 shows grids in which the points are equispaced in the direction normal to the airfoil surfaces.

Zones 3 and 4 are shown in Fig. 5. The grids for these zones are generated algebraically. Zone 3 contains zone 1 and, consequently, the stator. Zones 1 and 3 overlap each other and are also stationary with respect to each other. In fact, the inner boundary of zone 3 is contained within zone 1 and the outer boundary of zone 1 is contained within zone 3. This positioning of the boundaries is necessary for the transfer of information between zones 1 and 3. The relationship between zones 2 and 4 is similar to that between zones 1 and 3. Additionally, zones 3 and 4 abut each other along the patch boundary ABCD (Fig. 5). These two zones (3 and 4) slip past each other as the rotor airfoil moves downward. Zones 3 and 4 constitute a patched grid system. It is advantageous to use a patch boundary (as opposed to an area of overlay) where one system of grids moves relative to another system of grids because both time accuracy and conservation can be more easily controlled in patched-grid calculations.

An interesting feature of zones 3 and 4 as seen in Fig. 5 is that they do not align with each other. The segment AB of zone 4 does not seem to align with any part of the patch boundary of zone 3 and, similarly, the segment CD of zone 3 does not seem to align with any part of the patch boundary of zone 4. However, the periodicity boundary condition can be used to solve this problem, the result being that the segment AB is matched with the segment CD. Figure 6 shows all the zones that are used in the calculation. The relative positions of the boundaries of each zone are clearly shown.

Boundary Conditions

The use of multiple grids in simulating the flow over the rotor/stator configuration shown in Fig. 3 results in several computational boundaries. The boundary conditions used at each of these boundaries is briefly outlined below.

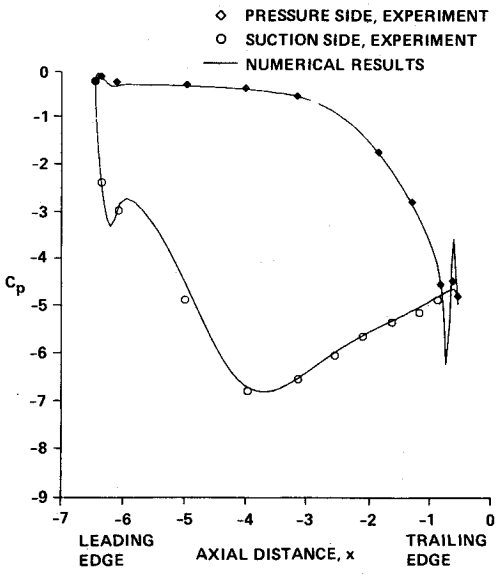

Fig. 7 Time-averaged pressure distribution on the stator.

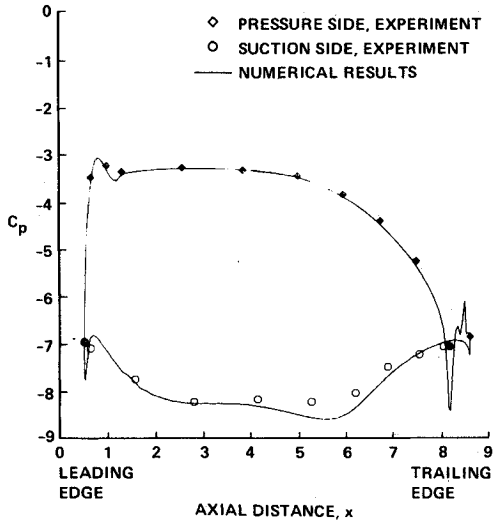

Fig. 8 Time-averaged pressure distribution on the rotor.

Natural Boundaries

The inner boundaries of the two "O" grids correspond to the airfoil surfaces; hence, the "no-slip" condition and the adiabatic wall condition (or wall temperature) are imposed at these boundaries. It should be noted that in the case of the rotor "no slip" does not imply zero velocity at the surface of the airfoil; instead, it means that the fluid velocity at the rotor surface is equal to the rotor speed. In addition to the no-slip condition, the derivative of the pressure normal to the wall surface is set to zero. The pressure derivative condition, adiabatic wall condition, and equation of state together yield

$$\frac{\partial \rho}{\partial n} = 0$$

$$\frac{\partial e}{\partial n} = \frac{u}{\rho}\frac{\partial \rho u}{\partial n} + \frac{v}{\rho}\frac{\partial \rho v}{\partial n}$$

where n is the direction normal to the airfoil surface. These boundary conditions are implemented in an implicit manner by using the following equation instead of Eq. (8) to update the grid points on the airfoil surfaces:

$$C(\tilde{Q}^{p+1}_{j,1} - \tilde{Q}^{p}_{j,1}) + D(\tilde{Q}^{p+1}_{j,2} - \tilde{Q}^{p}_{j,2}) = 0 \tag{13}$$

where

$$C = \begin{bmatrix} 1 & 0 & 0 & 0 \\ 0 & 1 & 0 & 0 \\ 0 & 0 & 1 & 0 \\ 0 & \alpha & \beta & 1 \end{bmatrix} \quad D = \begin{bmatrix} \theta & 0 & 0 & 0 \\ 0 & 0 & 0 & 0 \\ 0 & 0 & 0 & 0 \\ 0 & \alpha\theta & \beta\theta & \theta \end{bmatrix}$$

and

$$\theta = -\frac{J_{j,2}}{J_{j,1}}, \quad \alpha = -\frac{u_{\text{wall}}}{\rho_{\text{wall}}}, \quad \beta = -\frac{v_{\text{wall}}}{\rho_{\text{wall}}}$$

Equation (13) is an implicit, spatially first-order accurate implementation of the no-slip (adiabatic wall) condition (first-order accurate because the zero normal derivative condition is implemented using a two-point forward difference). A second-order accurate, three-point forward-difference corrector step is also implemented after each time step. It should be noted that Eq. (13) requires that the grid be orthogonal at the blade surfaces and that the Jacobians of the transformation $J_{j,1}$ and $J_{j,2}$ be independent of τ.

The left boundary of zone 3 is a subsonic inlet boundary. Three quantities need to be specified at this boundary. The three chosen for this study are the Riemann invariants[10,11]

$$R_1 = u + \frac{2c}{\gamma - 1}, \quad R_3 = \frac{p}{\rho^{\gamma}} \tag{14}$$

and the inlet flow angle which in this case is equivalent to

$$v_{\text{inlet}} = 0 \tag{15}$$

The fourth quantity (which is necessary to update the points on this boundary) is also a Riemann invariant

$$R_2 = u - \frac{2c}{\gamma - 1} \tag{16}$$

and is extrapolated from the interior of zone 3. The manner in which these boundary conditions can be implemented implicitly is described in Ref. 12.

The calculation assumes that there are an infinite number of rotor and stator airfoils in the positive and negative y directions in Fig. 3. Hence, a simple periodicity boundary condition is imposed on the upper and lower surfaces of zones 3 and 4. The implicit implementation of this boundary condition is straightforward and will not be discussed here. The right boundary of zone 4 is a subsonic exit boundary. A simple extrapolation procedure is used at this boundary. This boundary condition is implemented implicitly by using the equation

$$(\tilde{Q}^{p+1}_{j\max,k} - \tilde{Q}^{p}_{j\max,k}) - \frac{J_{j\max-1,k}}{J_{j\max,k}}(\tilde{Q}^{p+1}_{j\max-1,k} - \tilde{Q}^{p}_{j\max-1,k}) = 0 \tag{17}$$

instead of Eq. (8) to update the grid points. Whereas the use of Eq. (17) results in a stable calculation, it may be necessary to specify one condition (such as R_2 or the exit flow angle) to obtain accurate results in the vicinity of the exit boundary.

Overlap Boundary

The overlap boundary conditions used at the inner boundaries of zones 3 and 4 and the outer boundaries of zones 1

and 2 are simple. They are given by

$$(\tilde{Q}^{p+1} - \tilde{Q}^{p})_{\text{o.b.}} = 0 \tag{18}$$

where the subscript o.b. refers to the points on the overlap boundary. This is followed by an explicit, corrective, interpolation procedure at the end of each iteration wherein the values of Q^{p+1} along the outer boundaries of zones 1 and 2 are interpolated from the interior grid points of zones 3 and 4, respectively, and the values of Q^{p+1} along the inner boundaries of zones 3 and 4 are interpolated from the interior grid points of zones 1 and 2, respectively (the values of Q^{p+1} obtained from the implicit integration procedure along the overlap boundaries are discarded). The results in this study are obtained using a linear interpolation over triangles.

The boundary condition given by Eq. (18) is not the same as that given by

$$(\tilde{Q}^{n+1} - \tilde{Q}^{n})_{\text{o.b.}} = 0$$

Equation (18) [in addition to Eq. (8) in the interiors of the zones] allows $(\tilde{Q}^{n+1} - \tilde{Q}^{n})_{\text{o.b.}}$ to assume its right value when the iteration process is carried to convergence (in addition to the corrective interpolation procedure described above). Both time accuracy and a spatial accuracy consistent with the order of interpolation used are maintained at the overlap boundaries by using Eq. (18).

Patch Boundaries

The equations necessary to transfer information in a time-accurate, conservative manner across the patch boundary (ABCD in Fig. 5) along which zones 3 and 4 slip past each other have already been developed and tested in Refs. 3 and 4. The development of these equations is fairly involved and, therefore, in the interest of brevity, is not included here. Details of the patch-boundary condition used in this study can be found in Ref. 3.

Results

In this section, we present results obtained for the rotor/stator configuration shown in Fig. 3. These results were obtained by integrating Eq. (8) and the boundary conditions described in the previous section. Four iterations were performed at each time step. The magnitude of the maximum residual in the system was reduced by more than an order of magnitude at the end of the fourth iteration. Approximately five cycles (a cycle corresponds to the motion of the upper boundary of zone 4 from its current position to the position occupied currently by the lower boundary of zone 4) were required to eliminate the initial transients and to establish a solution that was periodic in time. The calculation was performed at a constant time-step value of 0.04 (the corresponding maximum CFL number in the grid system was approximately 250).

The dependent variables were nondimensionalized with respect to the ambient pressure p_∞ and density ρ_∞. This yields

$$u_\infty = M_\infty \sqrt{\gamma}$$

$$v_\infty = 0 \text{ (inlet flow is axial)}$$

where M_∞ is a reference Mach number. For the purpose of initializing the dependent variables in the four zones and also specifying the Riemann invariants R_1 and R_3, it was assumed that M_∞ was equal to 0.1. However, because the quantities prescribed at the inlet boundary were R_1, R_3, and the inlet flow angle and not the dependent variables themselves, the average Mach number at the inlet (when the solution became periodic in time) was found to be approximately 0.08. The velocity of the rotor airfoil ω was approximately 1.33 times the average inlet velocity (this is fairly close to the experimental value of 1.28).

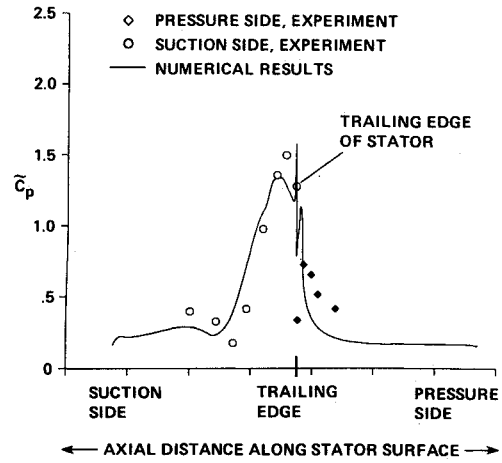

Fig. 9 Pressure amplitude distribution on the stator.

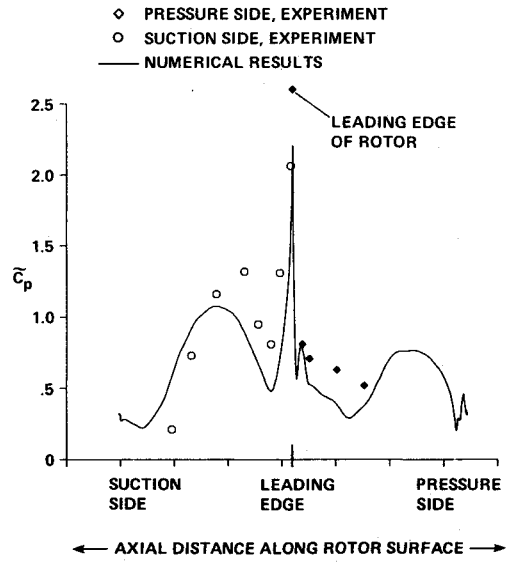

Fig. 10 Pressure amplitude distribution on the rotor.

The Reynolds number for the calculation was chosen to be 100,000/in. The Baldwin-Lomax turbulence model[13] was used to determine the eddy viscosity. The kinematic viscosity was calculated using Sutherland's law. The viscous terms were evaluated only in zones 1 and 2. It was assumed that because of the coarse grids in zones 3 and 4, the magnitudes of the viscous terms in these zones were negligible.

In the figures that follow, there are several comparisons made with experimental data. The following points must be kept in mind when evaluating these comparisons:

1) The airfoil geometry used in the numerical calculation is only an approximation to that used in the experiment (the actual configuration consisted of 22 stator airfoils and 28 rotor airfoils; the calculation was performed with 22 of each with an enlarged rotor geometry).

2) The rescaling of the geometry requires the modification of the Reynolds number to simulate equivalent conditions in the calculation; however, it is not clear how this modification should be effected.

3) The inlet conditions were reasonably close, but not identical, to those used in the experiment. Since the quantities specified at the inlet are not the dependent variables themselves, it is difficult to specify exactly such experimental inlet conditions as velocity and total pressure at the inlet. The specification of quantities (i.e., inlet velocity) may require an iterative procedure where the inlet values of the Riemann variables are continuously modified so that the

time-averaged numerical inlet conditions such as velocity and pressure match the time-averaged experimental inlet conditions.

4) The current analysis is only two-dimensional in nature, whereas the actual flow is three-dimensional.

5) The axial gap between the blades in the experiment was 15% of the average chord length. It is difficult to estimate the equivalent axial gap in the case of the modified rotor. The calculation was performed using an axial gap that was 15% of the average chord length.

Time-Averaged Pressures

Figure 7 shows the time-averaged pressure coefficient C_p as a function of the axial distance along the stator. The pressure coefficient is defined as

$$C_p = \frac{p_{\text{avg}} - (p_t)_{\text{inlet}}}{(\frac{1}{2})\rho_{\text{inlet}}\omega^2}$$

where p_{avg} is the static pressure averaged over one cycle, $(p_t)_{\text{inlet}}$ the average total pressure at the inlet, and ρ_{inlet} the average density at the inlet. There is a good agreement between theory and experiment. A small separation bubble was found on the trailing-edge circle of the stator in the numerical results. This is seen as a sharp dip and rise of C_p toward the trailing edge of the stator. The experimental data also indicate such a separation. However, the magnitude of the spatial pressure fluctuation obtained numerically may be suspect because the turbulence model was not tailored to yield accurate estimates of the eddy viscosity in such regions.

Figure 8 shows the time-averaged C_p distribution for the rotor. The agreement is good except in the minimum pressure region of the rotor ($4.0 \le x \le 7.0$). This difference between experimental and numerical results is probably because of three-dimensional effects (caused by the low aspect ratio of the airfoil). A small separation bubble was found near the trailing edge as in the case of the stator. The bubble is seen as a spatial fluctuation in pressure. Once again, the magnitudes of these fluctuations may be inaccurate. It is suspected that the increased mixing existing in the trailing-edge separation bubble will result in larger eddy viscosity values and smaller spatial pressure fluctuations in the real case (the sparsity of experimental points precludes any definite conclusions at the present time).

Unsteady Pressures

Figure 9 shows the magnitude of the temporal pressure fluctuation $\tilde{C}_p$ along the surface of the stator (plotted as a function of the axial distance). The quantity $\tilde{C}_p$ is defined as

$$\tilde{C}_p = \frac{p_{\max} - p_{\min}}{(\frac{1}{2})\rho_{\text{inlet}}\omega^2}$$

where $p_{\max}$ and $p_{\min}$ are the maximum and minimum pressures occurring over a cycle at a given point. The agreement between experiment and theory in Fig. 9 is fairly good considering that the rotor moving past the stator is much larger than the actual one. Figure 10 shows the $\tilde{C}_p$ distribution for the rotor. The comparison between experimental and numerical values is not as good as in the case of the stator. However, the numerical calculation does predict all the qualitative features shown by the experiment.

The periodic boundary conditions on the upper and lower boundaries of zones 3 and 4 result in a periodicity in time of the solution within these zones. The pressure and other dependent variables become periodic in time after the initial transients dissipate. Any numerical scheme (this includes the interior and boundary schemes) devised to calculate rotor/stator flow must be able to simulate this periodicity in time. To test this particular capability of the interior integration and boundary schemes, the pressure was monitored at selected locations of the stator. Figure 11a shows the locations at which the pressure was monitored and Figs. 11b–11d show the variation of pressure over three cycles, as a function of time, at these locations. The periodicity in time is clearly observed, thus demonstrating the capability of the method in simulating periodic time-dependent flows. The magnitude of the temporal pressure fluctuations varies and was found to be maximum at point B. Similar results were obtained for the rotor.

Figure 12 shows a three-dimensional plot of pressure as a function of time and position on the stator. To facilitate comparisons with a similar plot in Ref. 1, it has been plotted with the pressure decreasing in the upward direction (however, the plot in Ref. 1 does not contain the mean component of the pressure). This results in the low-pressure regions appearing as peaks and the high-pressure regions as valleys. The variation of pressure amplitude on the stator can be seen in Fig. 12. The largest amplitudes occur on the suction side and close to the trailing edge. The amplitudes at the leading edge and on most of the pressure side are very small. There is a gradual increase in amplitude as we move from the leading edge to the trailing edge on the suction side. Another interesting feature is the sudden change in

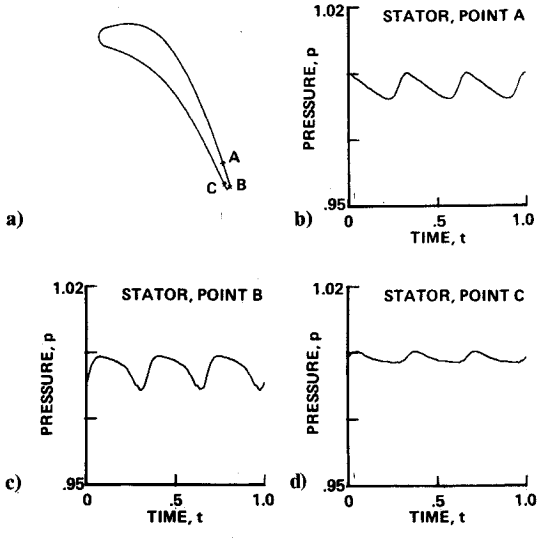

Fig. 11 Unsteady pressures on the stator: a) stator locations at which unsteady pressures were monitored; b) unsteady pressure at point A on the stator; c) unsteady pressure at point B on the stator; d) unsteady pressure at point C on the stator.

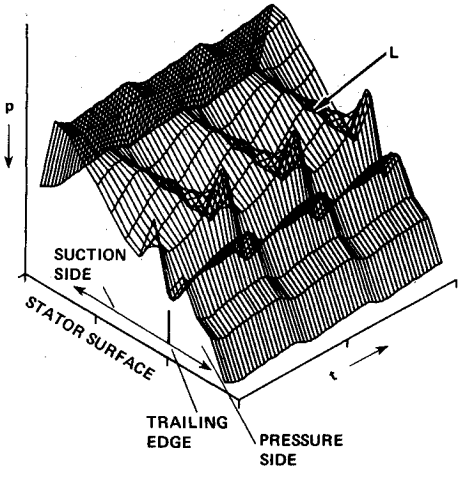

Fig. 12 Unsteady pressures on the stator surface.

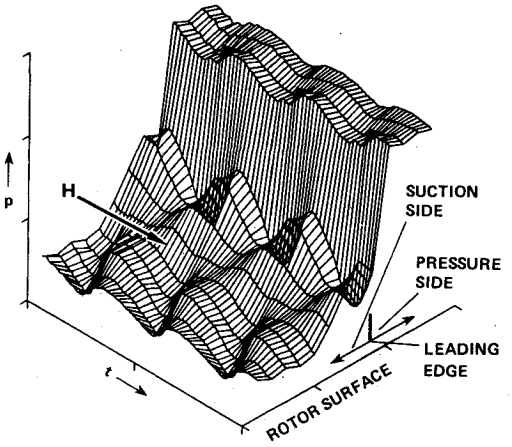

Fig. 13 Unsteady pressures on the rotor surface.

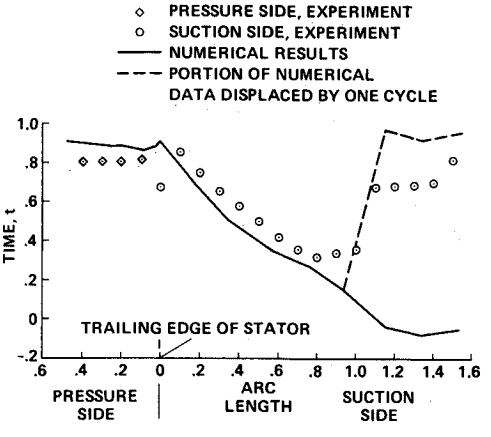

Fig. 14 Phase of the low-pressure peak seen in Fig. 12.

amplitude at the trailing edge as we move from the suction to the pressure side. Figure 12 also shows the phase shift that occurs in the low-pressure region L along the suction side. The low-pressure peaks close to the leading edge are almost 180 deg out of phase with respect to the peaks at the trailing edge. All of the features mentioned above agree qualitatively with the experimental data of Ref. 1 (not reproduced here).

Figure 13 shows the three-dimensional plot of unsteady pressures for the rotor. The pressures in this case are plotted with increasing value in the upward direction. The largest amplitudes occur at the leading edge and on the suction side. The pressure amplitudes are rather small at the trailing edge and all along the pressure surface. The amplitudes decay as we move away from the leading edge on the suction surface. There is also an abrupt change in amplitude as we move from the suction to the pressure side at the leading edge. An interesting feature that can be observed in Fig. 13 is the phase shift that occurs in the high-pressure region H as one moves away from the leading edge on the suction surface (the high-pressure peak occurs at different times). As in the previous case, the numerical data agree qualitatively with the experimental data.

While it is difficult to make detailed comparisons of the unsteady pressure surfaces obtained experimentally and numerically, it is a relatively simple matter to make comparisons of any one particular feature on the pressure surface. Figure 14 shows the phase of the low pressure region L (Fig. 12) for the stator. The plot shows the time at which the low-pressure peak occurs as a function of arc length along the stator. The initial positions ($t=0$) for the rotor and stator are shown in Fig. 3 ($t=0$ corresponds to the instant when the centers of the trailing-edge circle of the stator and

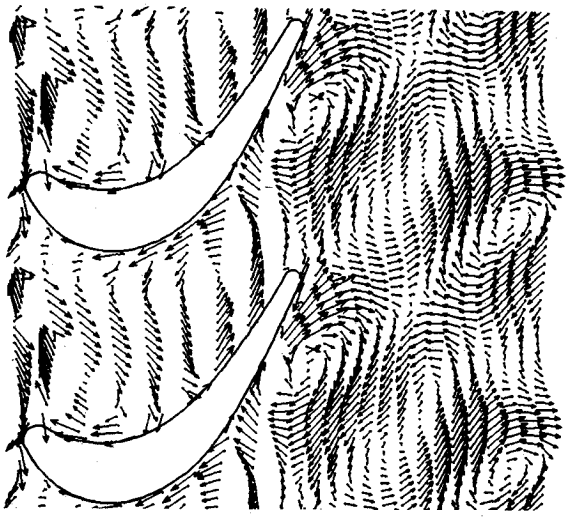

Fig. 15 Unsteady velocity vectors depicting the unsteady shedding of vortices by the system.

the leading-edge circle of the rotor are aligned with each other). The experimental values are below the numerical values on the pressure side and above the numerical values on the suction side. This is because the frequency at which the rotor airfoils pass the stator airfoils in the experiment is different from the frequency at which they do so in the calculation (there are fewer rotor airfoils in the calculation). This happens despite the fact that the tangential velocity ω of the rotor airfoils is the same in both the experiment and the numerical calculation. While the numerical data can be modified to take into effect the differences in airfoil passing frequency (between the experiment and the calculation), truly accurate phase estimates can be obtained only with a multiple airfoil calculation.

Unsteady Velocity Vectors

Figure 15 shows the unsteady velocity vectors at selected points in the flowfield at a particular instant in time. These unsteady velocities were obtained by subtracting the time-averaged (averaged over one cycle) velocity vector at each grid point from the instantaneous velocity vector. The vectors in Fig. 15 show the direction and relative magnitude (the lengths of the vectors were scaled appropriately to obtain the best visual effect) of the unsteady velocity component. The main feature of Fig. 15 is the unsteady shedding of vortices by the system because of the periodic lift on the rotor airfoils. The periodicity of the lift requires that vortices of equal and opposite strength (referred to as positive and negative vortices hereafter) be shed every cycle. Figure 15 shows two negative vortices (from two different cycles) and one positive vortex, thus clearly demonstrating the mechanism involved in producing a periodic loading on the airfoils. The positive vortex is seen to be more diffuse than the negative vortex. This is because of the nature of the velocity profile at the rotor inlet; the velocity increases gradually as we move from the pressure side of a stator airfoil to the suction side of the stator below it and then decreases and increases rapidly as one moves across the wake of the stator.

Mach Number Contours

Figures 16–18 depict Mach number contours at various positions of the rotor with respect to the stator. Although the calculation was performed with only two airfoils, for the sake of clarity these contour plots depict several airfoils. The information regarding the additional airfoils is obtained from the periodicity condition. The thickening of the boundary layer as we move from the leading to the trailing edges of

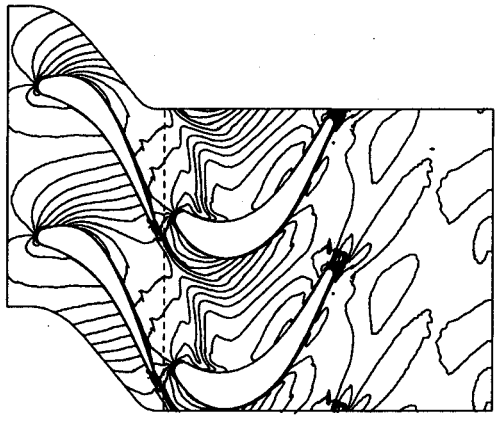

Fig. 16 Mach number contours ($t = 0.00$).

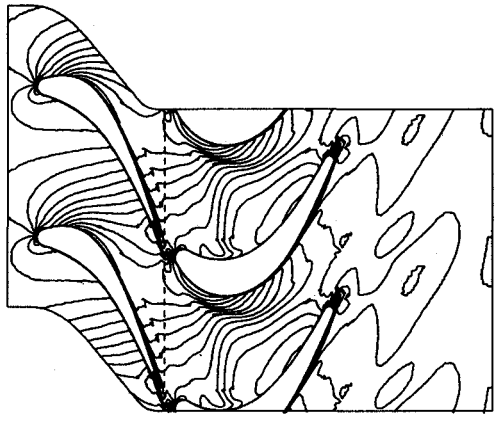

Fig. 17 Mach number contours ($t = 0.25$).

the rotor and stator airfoils is evident. The wakes associated with the airfoils are also clearly seen. In Fig. 16, the stator wake is below the rotor. In Figs. 17 and 18, an interaction between the stator wake and the rotor is observed.

Figures 16–18 show contour lines that are smooth and continuous across the patch boundary. However, this is not the case with the contour lines in the vicinity of the overlap boundaries. It was found that the overlap boundaries gave rise to small-amplitude, high-frequency oscillations in the pressure and density values close to the overlap boundaries. The low Mach numbers in the calculation tended to sustain these oscillations because of the decoupling of the continuity, momentum, and energy equations. It is suspected that the overlap boundary procedure gives rise to these oscillations because conservation is not strictly enforced at these boundaries (the patch boundary condition, on the other hand, is fully conservative).

Computing Time Requirements

The calculation presented in this study was performed with approximately 25,000 grid points (approximately 6250 grid points per zone). Four iterations were used at each time step in order to reduce the maximum residue in the continuity equation by more than an order of magnitude and 2000 time steps were used per cycle. For this choice of algorithmic parameters, the code required 3 h of computing time per cycle on the CRAY-XMP. The solution took approximately five cycles to become periodic in time and required 15 h to calculate.

One of the main reasons for the excessive amount of computing time needed for the calculation is the restrictive time-step constraint imposed by stability requirements. The code was found to be unstable for CFL numbers larger than 500

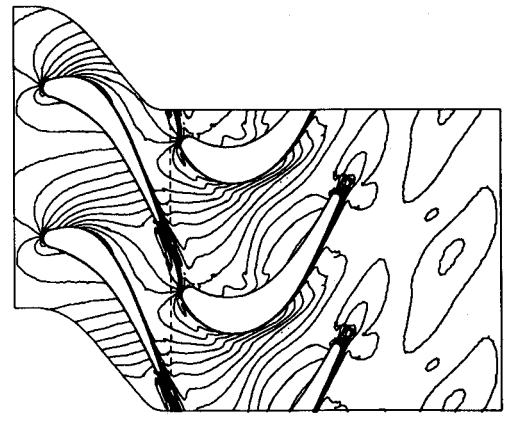

Fig. 18 Mach number contours ($t = 0.50$).

(the current calculation was performed at a CFL number of approximately 250) in spite of the implicit nature of the algorithm. The stability constraint was found to be far more restrictive than the constraint imposed by time-accuracy considerations. More recent test calculations with improved linearization and zoning techniques have resulted in reducing the time requirements per cycle by a factor of five.

Alternate Boundary Conditions

The prescription of three Riemann invariants at the inlet boundary is both physically right and numerically stable. Although they are found to be numerically stable in the present calculation, extrapolating all four dependent variables from the interior to the exit boundary does not uniquely specify the mass flow and may lead to nonunique solutions in other situations. Hence, the boundary conditions were modified to enforce the total pressure at the inlet (instead of entropy as in the previous case) and to enforce the static pressure at the exit. The results obtained were essentially the same as those presented earlier. Details of this calculation will be presented in a forthcoming article.

Areas for Future Research

There are several differences between the experimental conditions and the conditions under which the numerical calculation was performed. Chief among them is the difference in the number of rotor airfoils and the size of these airfoils. To simulate accurately the experimental data, one needs to use a minimum of 11 stator airfoils and 14 rotor airfoils (in order to be able to implement the periodicity boundary condition at the proper locations). Such a calculation would be extremely time consuming. A better approach, and one that would justify the necessity for a multiple airfoil calculation, would be to use four stator airfoils and five rotor airfoils, a total of nine airfoils. The ratio of the number of airfoils (rotor vs stator) for this configuration is $5/4 = 1.250$, whereas the ratio in the real case is $28/22 = 1.273$. Hence, the factor by which the rotor airfoils will have to be enlarged is $1.273/1.250 = 1.018$ instead of the factor 1.273 used in the present calculation. The nine airfoil calculation should yield better phase relationships and pressure amplitudes.

The second problem that needs to be addressed is the turbulence model. Experience indicates that an algebraic turbulence model does not accurately predict eddy viscosities in regions of separation and in wakes without requiring extensive "fine-tuning" of the model. Hence, it is important to use a more generally applicable turbulence model such as the two-equation models. Preliminary investigations show that the k–ϵ turbulence model[14] yields more accurate estimates of the eddy viscosity in the separation regions near the trailing edges of the blades and, hence, results in smaller spatial pressure fluctuations.

The conservative treatment of overlap boundaries is much more difficult than the conservative treatment of patched-grid boundaries. For this reason, the overlap boundaries in the present study were not made fully conservative. In the author's opinion, this is the cause for the high-frequency oscillations in the dependent variables close to the overlap boundaries. This problem may worsen in situations where there are flow discontinuities passing through the overlap boundaries. Hence, it is preferable either to use only patched-grids (which have already been made conservative in Refs. 2–4) for multiple-grid calculations or to develop a simple way of treating overlay boundaries in a conservative manner.

The improvements mentioned above are necessary in order to build a reliable rotor/stator analysis tool. Current research is therefore being focused on building an unsteady, Navier-Stokes, multiple-airfoil, patched-grid code that uses a two-equation turbulence model.

Conclusions

An unsteady, thin-layer, Navier-Stokes code to study rotor/stator interaction problems has been developed. The code uses patched and overlaid grids that move relative to each other to be able to simulate the motion of the rotor airfoils with respect to the stator airfoils. The code was used to simulate subsonic flow past a rotor/stator configuration for which considerable experimental data exist.

The numerical results were compared with experimental data. The agreement was found to be good in the case of time-averaged surface pressure distributions. The comparison between pressure amplitudes and phase relationships was not quite as good. This is most probably because of the several differences between the experimental conditions and the ones used for the numerical calculation, such as the modified rotor geometry that is used in the calculation.

Several problem areas will have to be addressed in the future. The most important of these are 1) the turbulence model, 2) the use of multiple airfoils in the calculation, 3) the development of conservation principles for overlap boundaries, and 4) the use of patched grids alone in simulating rotor/stator flows and a possible increase in the number of zones.

Acknowledgments

I would like to thank Dr. D. S. Chaussee, Dr. T. H. Pulliam, and Dr. J. L. Steger of NASA Ames Research Center for the many helpful suggestions they provided during this investigation. I am especially grateful to Dr. R. P. Dring of United Technologies Research Center for the help rendered in interpreting the numerical data and for providing the blade geometry and experimental data.

References

[1]Dring, R. P., Joslyn, H. D., Hardin, L. W., and Wagner, J. H., "Turbine Rotor-Stator Interaction," *Journal of Engineering for Power,* Vol. 104, Oct. 1982, pp. 729–742.

[2]Rai, M. M., "A Conservative Treatment of Zonal Boundaries for Euler Equation Calculations," *Journal of Computational Physics,* Vol. 62, Feb. 1986, pp. 472–503.

[3]Rai, M. M., "An Implicit Conservative Zonal Boundary Scheme for Euler Equation Calculations," *Computer and Fluids,* Vol. 14, No. 3, 1986, p. 295–319.

[4]Rai, M. M., "A Relaxation Approach to Patched-Grid Calculations with the Euler Equations," *Journal of Computational Fluids,* Vol. 66, Sept. 1986, pp. 99–131.

[5]Benek, J. A., Steger, J. L., and Dougherty, F. C., "A Flexible Grid Embedding Technique with Application to the Euler Equations," AIAA Paper 83-1944, July 1983.

[6]Beam, R. M. and Warming, R. F., "An Implicit Factored Scheme for the Compressible Navier-Stokes Equations," AIAA Paper 77-645, June 1977.

[7]Rai, M. M. and Chakravarthy, S. R., "An Implicit Form for the Osher Upwind Scheme," *AIAA Journal,* Vol. 24, May 1986, pp. 735–743.

[8]Pulliam, T. H. and Steger, J. L., "On Implicit Finite-Difference Simulations of Three-Dimensional Compressible Flow," *AIAA Journal,* Vol. 18, Feb. 1980, pp. 159–167.

[9]Steger, J. L. and Sorenson, R. L., "Automatic Mesh-Point Clustering Near a Boundary in Grid Generation with Elliptic Partial Differential Equations," *Journal of Computational Physics,* Vol. 33, No. 3, Dec. 1979, pp. 405–410.

[10]Salas, M. D., Jameson, A., and Melnik, R. E., "A Comparative Study of the Nonuniqueness Problem of the Potential Equation," AIAA Paper 83-1888, July 1983.

[11]Pulliam, T. H. and Steger, J. L., "Recent Improvements in Efficiency, Accuracy, and Convergence for Implicit Approximate Factorization Algorithms," AIAA Paper 85-0360, Jan. 1985.

[12]Rai, M. M. and Chaussee, D. S., "New Implicit Boundary Procedures: Theory and Application," *AIAA Journal,* Vol. 22, Aug. 1984, pp. 1094–1100.

[13]Baldwin, B. S. and Lomax, H., "Thin Layer Approximation and Algebraic Model for Separated Turbulent Flow," AIAA Paper 78-257, Jan. 1978.

[14]Chien, Kuei-Yuan, "Predictions of Channel and Boundary-Layer Flows with a Low-Reynolds-Number Turbulence Model," *AIAA Journal,* Vol. 20, Jan. 1982, pp. 33–38.